View Article Online
View Journal

Journal of
Materials Chemistry A
Materials for energy and sustainability

This article can be cited before page numbers have been issued, to do this please use: M. Bai, M. Zhong, W. Shen, J. Zhang and S. Guo, *J. Mater. Chem. A*, 2025, DOI: 10.1039/D4TA07788A.

ROYAL SOCIETY
OF **CHEMISTRY**

rsc.li/materials-a

View Article Online
DOI: 10.1039/D4TA07788A

ARTICLE

Free-standing graphene films decorated with lithiophilic particles as host electrode for lithium plating/stripping in anode-less lithium metal batteries

Received 00th January 20xx,
Accepted 00th January 20xx

DOI: 10.1039/x0xx00000x

Mingliang Bai,[a] Min Zhong,*[a] Wenzhuo Shen,[a] Jiali Zhang,[a] and Shouwu Guo*[a]

The host electrode is key to the lithium plating and stripping in anode-less lithium metal batteries. In the work, we fabricate a series of free-standing porous graphene films decorated with the lithiophilic particles of AlN@Li_3N, MgF_2, Li_2CO_3, and the Mg-Li alloy foil, and explore systematically their electrochemical properties as lithium-host materials in anode-less lithium metal batteries. We characterize the structures and morphologies of the multifunctional graphene films before, after, and in the course of the lithium plating/stripping, to elaborate the effects of different components in the film on the lithium plating/stripping. We demonstrate that the graphene sheets serve as optimal host for lithium plating/stripping, the AlN@Li_3N, MgF_2, and Li_2CO_3 enable the formation of inorganic LiF and Li_3N-rich solid electrolyte interphase, and the Mg-Li alloy foil makes up for the lithium loss during the long-term cycling. The anode-less lithium metal batteries with the as-obtained graphene film as host electrode, NCM811 as cathode, and carbonate-based electrolyte exhibit excellent electrochemical performances, which capacity retention can reach to ~ 60 % after 120 cycles at 1.93 mA cm^{-2}.

1. Introduction

Lithium-ion batteries (LIBs) have seen great developments during last decades, but the energy density of conventional LIBs falls behind the iterations of the electric vehicle and other energy storage devices, which require the LIBs density > 350 Wh kg^{-1} at the cell level.[1-3] As anode, lithium metal shows a high specific capacity of ~ 3860 mAh g^{-1}, and a low redox potential of -3.04 V *vs.* standard hydrogen electrode.[4] Thus, in recent years, the LIBs with lithium metal as anode, termed as lithium metal batteries (LMBs), have been considered as alternatives of traditional LIBs. However, there are still some drawbacks blocking the practical application of LMBs.[5] For instance, the irregular lithium deposition, such as dendrites, causes quick battery failure.[6] The high active lithium reacts with the electrolyte, causing unexpected consumptions of both lithium and the electrolyte that lead to a fast capacity fading.[7] Therefore, several protocols have been developed to overcome the obstacles, including the host electrode designs,[8, 9] the solid electrolyte interphase (SEI) modification,[10, 11] and the component innovation of electrolyte.[12, 13]

Fairly saying, typical LMBs reported so far show lower energy densities than LIBs because excessive lithium used.[14] To further improve the energy density of LMBs, anode-less lithium metal batteries (AL-LMBs) have been proposed, which has low N/P ratio (ratio of anode to cathode in capacity) of ~ 0-1.[15, 16] However, lacking of proper electrolyte and host electrode for lithium plating/stripping, AL-LMBs still suffer from rapid capacity loss. For example, an AL-LMB with Cu||NCM111 configuration shows a capacity retention of only 23 % after the initial cycle.[17] To explore proper host electrodes for lithium plating/stripping in AL-LMBs, a series of three-dimensional networked host materials have been studied, which in principle can disperse the local surficial current density, and thus can slow the growth of dendrite.[18] Among them, carbonaceous materials including carbon fibers,[19] carbon tubes,[20] carbon cloth,[21] and graphene[22] have been used often, because of their availability and easy for chemically functionalization. However, the carbonaceous hosts exhibit practically poor lithiophilicity, and the morphology of the as-plated lithium is hard to be controlled.[21] Hence, the lithiophilic particles are induced often into carbonaceous host.[23] For example, a graphene skeleton decorated with ZnO nanosheets was prepared as host electrode for lithium plating/stripping.[24] Additionally, lithiophilic designs can also incorporate interface regulation, such as using TiN-decorated carbon fibres as a host electrode, which promotes the formation of a Li_3N-rich SEI.[25] Nevertheless, it is worth to point out that as host electrode for lithium plating/stripping, the coulombic efficiencies (CEs) of most carbonaceous materials including the graphene derivatives remain to be improved once the N/P ratio is near to 0.[26]

In the work, we design and fabricate a series of free-standing thin films as host electrodes for lithium plating/stripping in AL-LMBs, using graphene sheets decorated with the lithiophilic inorganic particles, and an Mg-Li alloy foil.

---

[a] *Department of Electronic Engineering, School of Electronic Information and Electrical Engineering, Shanghai Jiao Tong University, Shanghai 200240, China. Email: zomi@sjtu.edu.cn (M. Zhong), swguo@sjtu.edu.cn (S. Guo)*

† Supplementary Information available: additional XRM, SEM, and TEM images, additional nitrogen adsorption results; additional XPS spectra, particle size distribution, stress-strain, and ICP results; and additional electrochemical results of half-cells and full-cells, et. See DOI: 10.1039/x0xx00000x

View Article Online
DOI: 10.1039/D4TA07788A

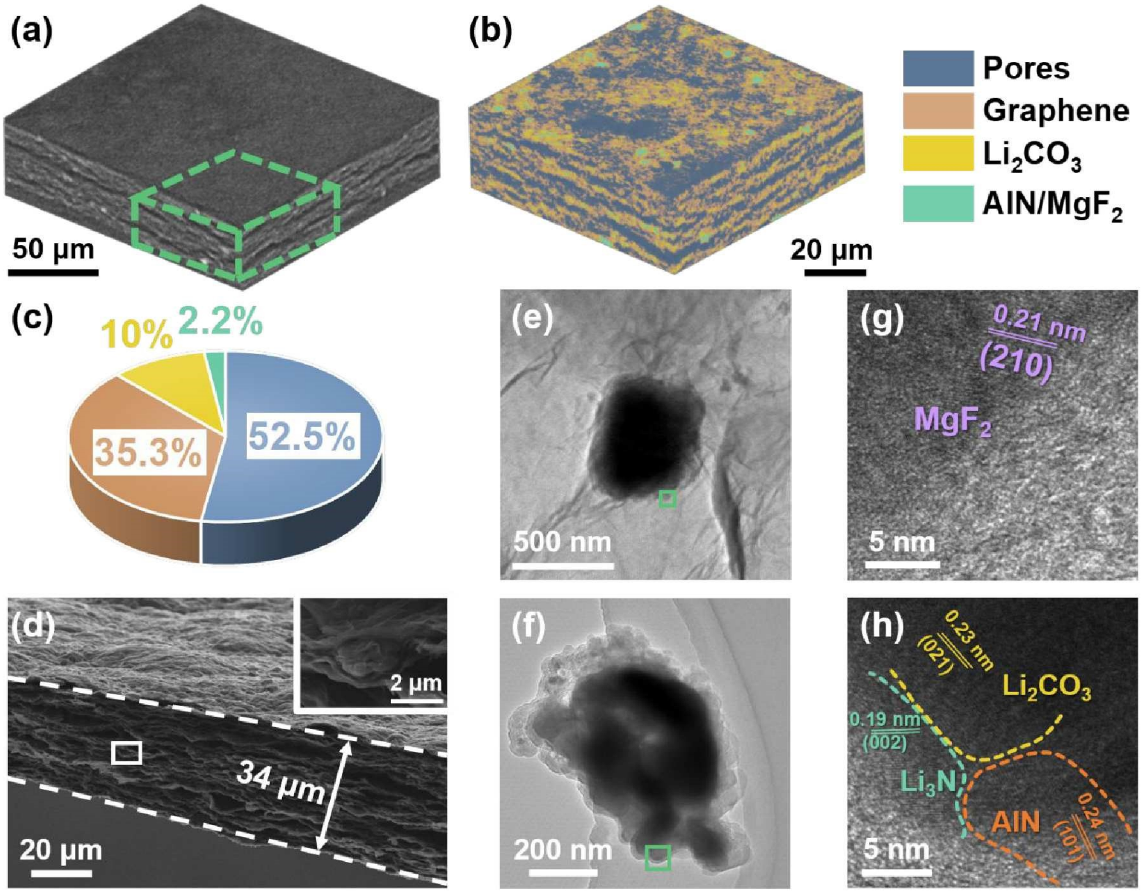

Fig. 1 (a) 3D XRM reconstructed images and (b) ROI distribution in the green box of LAG film. (c) Volumetric ratios of different components in LAG film. (d) Cross-sectional SEM image of LAG film, with the inset high magnified image. (e, f) TEM images of LAG film. (g, h) HRTEM images of the green sites in (e, f).

Predictably, the as-obtained graphene films should be able to enhance the coulombic efficiency and reversibility of lithium plating/stripping owing to: (1) the large porosity and uniform pore distribution which compacts the lithium deposition; (2) the lithiophilic inorganic particles that guide the lithium nucleation; (3) the Mg-Li alloy foil that makes up for the lithium loss; and (4) the *in-situ* formation of LiF and Li_3N which stabilize the interface between the electrolyte and electrode. The compositions, structures, and morphologies of the thin graphene films before, after, and even during lithium plating/stripping are characterized complementarily with X-ray microscopy (XRM), X-ray photoelectron spectroscopy (XPS), scanning electron microscopy (SEM), and high-solution transmission electron microscopy (HRTEM). The electrochemical properties of the as-obtained thin films as host electrode for lithium plating/stripping are evaluated both in half-cells and full-cells in commercial carbonate-based electrolyte. The underneath mechanisms are discussed systematically. As will be shown, using the as-fabricated free-standing thin graphene film as host electrode, $LiNi_{0.8}Co_{0.1}Mn_{0.1}O_2$ (NCM811) as cathode, the AL-LMB shows capacity retentions of ~ 60 % after 120 cycles with an average CE of ~ 99.4 % at an areal capacity of 3.86 mAh cm^{-2} and current density of 1.93 mAh cm^{-2}.

2. Results and discussion

2.1. Preparation and characterization of the graphene films decorated with lithiophilic inorganic particles.

The detailed preparation procedure of the free-standing graphene films decorated with and without inorganic (lithiophilic) particles, abbreviated as LAG and AG film, are summarized in the experimental part. The three dimensional (3D) morphology of the as-obtained LAG film is first characterized with X-ray microscopy (XRM) imaging followed by a structure reconstruction. To do it, the slices of the film are obtained through XRM imaging, seeing Fig. S1†. Subsequently, the slices are reconstructed through a software (*Dragonfly*), seeing Fig. 1a and a Movie in supporting information.[27] Meanwhile, four grey-scale density levels are recognized, the high (>3 g cm^{-3}), medium (>2 g cm^{-3}), low (>1 g cm^{-3}), and zero density regions are assigned to AlN/MgF_2, Li_2CO_3, graphene sheets, and pores, respectively. Accordingly, four regions of interest (ROIs) are created based on grey-scale divisions. The distinct peak at ~ 0 grayscale corresponds to the pores with

View Article Online
DOI: 10.1039/D4TA07788A

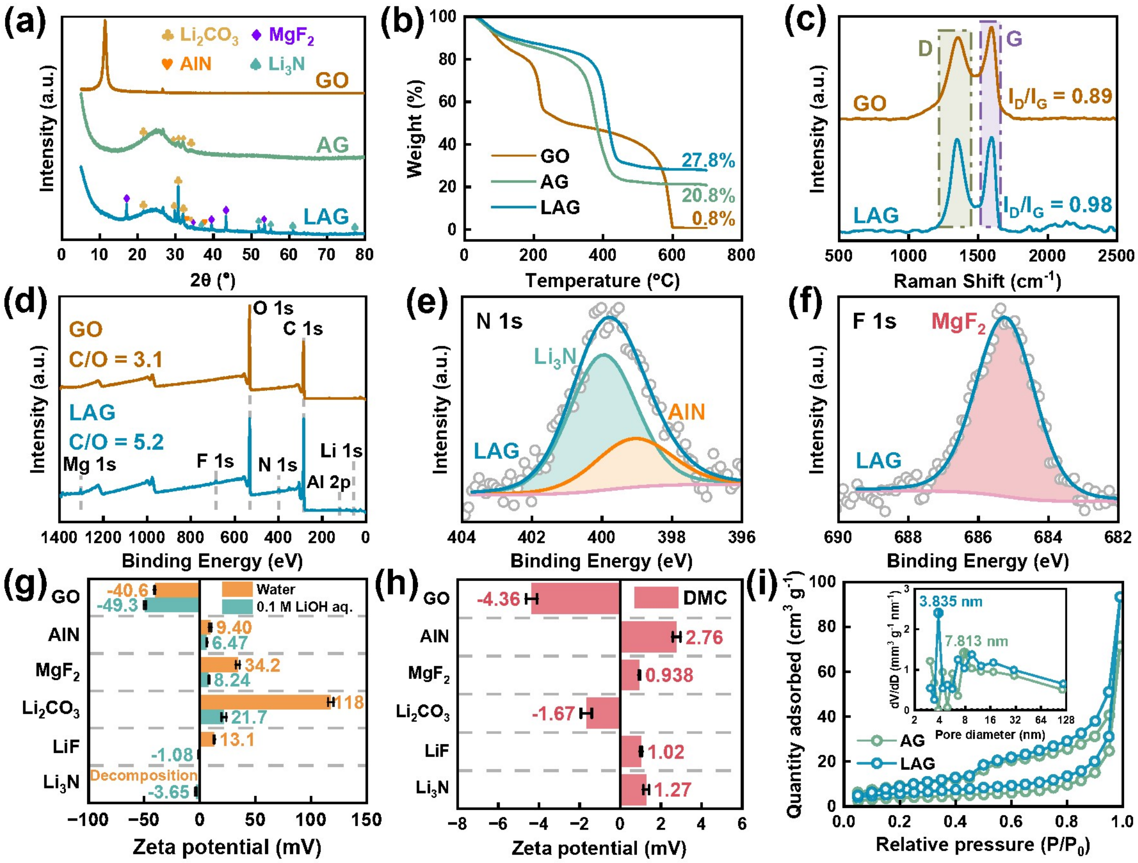

Fig. 2 (a) XRD patterns and (b) TGA curves of GO, AG, and LAG films. (c) Raman and (d) XPS survey spectra of GO and LAG films. (e-f) Deconvoluted XPS spectra of N 1s and F 1s of GO and LAG films, respectively. (g, h) Zeta potentials of GO, AlN, MgF_2, Li_2CO_3, LiF, and Li_3N in water, 0.1 M LiOH aqueous solution, and DMC, respectively. (i) Nitrogen isothermal adsorption curves of AG and LAG films, with the inset image of mesoporous distributions.

contrast-to-noise ratio between the pores and graphene of ~ 2.1 (Fig. S2†), which is considered to represent good contrast.[28] As illustrated in Fig. 1b, the LAG film is filled with plenty of micro-scale pores, originated most probably from the interconnection of graphene sheets. The volumetric and areal ratios of pores are calculated through ROI analysis, which are of 52.5 % and 49.5 %, respectively (Fig. 1c and S3†). The average sizes of the as-decorated particles are a few micrometers in diameter, which are consistent well with the original particle sizes of AlN and MgF_2, respectively (Fig. S4†). Fig. 1d shows the cross-sectional SEM images that the thin film is of 34 μm thick, and contains well-distributed particles, which are in consistent well with the aforementioned XRM data and the Energy dispersive spectrometer (EDS) mappings (Fig. S5†). On the contrary, AG film has an uneven porous structure shown in Fig. S6†. As depicted in Fig. 1e-g, the lattice fringes of as-decorated inorganic particles on graphene sheets are observed through HRTEM, including 0.24, 0.23, and 0.21 nm matching to $d_{(101)}$ of AlN, $d_{(021)}$ of Li_2CO_3, and $d_{(210)}$ of MgF_2, respectively. Besides as-loaded AlN and MgF_2, Li_2CO_3 generates most probably from the reaction of residual LiOH with CO_2 released during thermal treatment of graphene oxide (GO), which is the most common inorganic species in SEI to bear the huge volume fluctuation and accelerate the diffusion kinetics of Li^+.[29] Interestingly, $d_{(002)}$ of Li_3N is also detected (0.19 nm), which might be from the reaction between AlN and LiOH in the fabrication procedures ($AlN + 3LiOH \rightarrow 3Li_3N + Al(OH)_3$).

The structure of the LAG film was also characterized with X-ray powder diffraction (XRD). As shown in Fig. 2a, the weak and broaden XRD peaks of the aggregated graphene sheets,[30, 31] AlN (PDF#70-2543), and MgF_2 (PDF#70-2742), can be detected. Besides, the peaks of Li_3N (PDF#78-2005) and Li_2CO_3 (PDF#83-1454) are also observed, demonstrating the *in-situ* formation of Li_3N and Li_2CO_3. The thermogravimetric analysis (TGA) curves, Fig. 2b, show that ~ 20 *wt.* % of Li_2CO_3, ~ 7 *wt.* % of both AlN@Li_3N and MgF_2 are loaded on the LAG film. Fig. 2c shows the intensity ratio of D (~ 1350 cm^{-1}) to G (~ 1600 cm^{-1}) bands (I_D/I_G) of Raman spectrum of LAG film is higher than that of raw GO, revealing more defects accumulated on the graphene sheets in LAG film that on the other hand may afford more nucleation and storage sites for lithium metal.[22] Although the Raman signals from Li_2CO_3 at 712, 747, and 1459 cm^{-1} were difficult to distinguish, the ATR-IR spectra in Fig. S7† indicates the existence of Li_2CO_3 in LAG film. [32]

View Article Online
DOI: 10.1039/D4TA07788A

To evaluate the chemical states of different components within LAG, XPS measurements are conducted. The survey XPS spectra, Fig. 2d, show that the atomic ratio of C to O increases after thermal reduction. The hyperfine C 1s and O 1s spectra (Fig. S8†) verify that the reduction of GO and formation of Li_2CO_3. The N 1s peaks at 399.0 and 399.9 eV, Fig. 2e, demonstrate the existences of AlN and Li_3N. The formation of Li_3N accounts for that the as-decorated AlN reacts also with the LiOH during the LAG preparation, and the as-generated Li_3N seems attached on the surfaces of AlN particles. As depicted in Fig. 2f, the strong F 1s XPS peak at 685.3 eV reveals the successful decoration of MgF_2 particles on the graphene sheets. The Li 1s XPS peaks at 55.1 and 55.5 eV (Fig. S9†) confirm further the existences of both Li_3N and Li_2CO_3 in LAG film. The atomic proportions estimated from hyperfine XPS spectra are summarized in Table S1†. These results prove undoubtedly the reduction from GO to graphene sheets, the successful loading of AlN and MgF_2 particles, and the *in-situ* generation of Li_3N and Li_2CO_3 in the LAG film.

To understand the interactions among different components within the LAG film, the Zeta potentials of GO, AlN, MgF_2, Li_2CO_3, LiF, and Li_3N are measured in water, 0.1 M LiOH aqueous solution (pH = 13), and dimethyl carbonate (DMC), respectively. As shown in Fig. 2g, GO sheets show always the large negative potentials in water and 0.1 M LiOH aqueous solution, while AlN, MgF_2 and Li_2CO_3 have positive potentials in water and 0.1 M LiOH aqueous solution, which demonstrates that the electrostatic interaction drives the decorations of AlN, MgF_2 and Li_2CO_3 onto GO surface. For Li_3N, although being affected by hydrolyzation in water, it shows a weak negative potential (-3.65 mV) in 0.1 M LiOH aqueous solution (Fig. S10†). This means that the as-produced Li_3N may hardly exist alone, but can be attached on the positively charged surface of AlN particles. In DMC, as shown in Fig. 2h, GO sheets have still negative potential (-4.36 mV), AlN and MgF_2 show the positive potentials, meaning that even in DMC, common solvent for electrolyte in LIBs, the AlN and MgF_2 can be stably decorated on the GO surface. Additionally, the Zeta potentials of LiF, Li_3N, and Li_2CO_3 in DMC are also measured, which are -1.67, -1.02, and 1.27 mV, respectively. Obviously, LiF and Li_3N can still being attached on the graphene sheets with electrostatic interaction in DMC, which should be beneficial for the high quality SEI formation.[33, 34]

Nitrogen isothermal adsorption measurements are performed, and the multi-point Brunauer-Emmett-Teller (MBET) and Barrett-Joyner-Halenda (BJH) methods are used for surface-area calculations and mesopore analysis. Notably, LAG film has larger MBET surface area and mesopore volume (Fig. S11†), and rich porous features with narrower mesopore distribution (Fig. 2i). These are fully in agreement with the areal and volumetric analyzing results by 3D XRM reconstruction described above. The large surface area and pore volume could afford the LAG film with adequate spaces for lithium plating. The narrow mesopore distribution, and the small pore size should be conducive to constrain lithium deposition to achieve reversible lithium plating/stripping. As shown in Fig. S12†, in contrast to the AG film, the LAG film shows a higher mechanical strength, which might accommodate the volumetric variation during lithium plating/stripping. As depicted in Fig. S13†, the LAG film also displays the relatively lower contact angles with both water (~ 27 °) and DMC (~ 7 °), showing the better wettability.

2.2. Lithium plating and stripping performance of LAG film.

To investigate lithium plating/stripping performances of LAG films, a series of coin half-cells were assembled using Cu foil, AG, and LAG films as host electrodes, lithium foil as counter electrode, and commercial carbonate-based electrolyte (1 M $LiPF_6$ in ethylene carbonate (EC) /diethyl carbonate (DEC) /dimethyl carbonate (DMC) (1/1/1, in *vol.*) with 10% (in *vol.*) fluoroethylene carbonate (FEC)). As shown in Fig. 3a, to observe the lithium nucleation process, a small current density is applied first. Clearly, Cu shows the highest nucleation overpotential (~ 61 mV) for lithium plating, because of its intrinsic lithiophobic surface.[35] AG shows relative low lithium nucleation overpotential of ~ 5.9 mV, because its porous multilayer structure could induce lithium nucleation on graphene sheets. The LAG delivers the lowest nucleation overpotential of ~ 4.4 mV for lithium plating, the reason might be that it not only has porous multilayer graphene structure, but also contains lithiophilic AlN@Li_3N and MgF_2 particles. Fig. S14† shows a potential *versus* ultimate areal capacity curve of LAG film. The lithium plating process on LAG film is steady, and an extraordinarily large areal capacity of 30 mAh cm^{-2} can be achieved, which is actually higher than most of lithium hosts reported in the literature.[18] This result reveals the great lithium storage capacity of LAG film, indicative of its large pore volume and surface area. Besides the nucleation overpotentials, coulombic efficiency (CE), and potential hysteresis, the potential difference between real plating and ideally balanced deposition potential (0 V *vs.* Li^+/Li), are considered as the main factors affecting the lithium deposition.[36, 37] The CEs of aforementioned coin half-cells during long-term cycling at 1 mA cm^{-2} and 1 mAh cm^{-2} are shown in Fig. 3b, and the corresponding potential hysteresis are calculated and displayed in Fig. 3c. The CE for lithium plating/stripping on Cu drops quickly after a few cycles accompanied with the fast potential hysteresis increasing, and the coin half-cell fails after < 50 cycles, hinting the possible short-circuit caused probably by adverse lithium dendrite formation, and the electrolyte consumption through the side-reactions.[38] AG film delivers better lithium plating/stripping properties, including the stable potential hysteresis about ~ 30 mV, high CE about ~ 96.7 %, and longer cycle life over 250 cycles, because of its porous structure. In contrast, the LAG film exhibits the longest and most stable lithium plating/stripping cycling performance compared to Cu and AG. After 400 cycles, the average CE of LAG remains over ~ 98.6 %, and the average potential hysteresis is as low as of ~ 27 mV without an obvious increase (Fig. S15a and b†). As illustrated in Fig. S16a and b, the galvanostatic charge-discharge (GCD) curves of LAG film show that the lithium plating/stripping potential platforms are almost overlapped during 400 cycles,

View Article Online
DOI: 10.1039/D4TA07788A

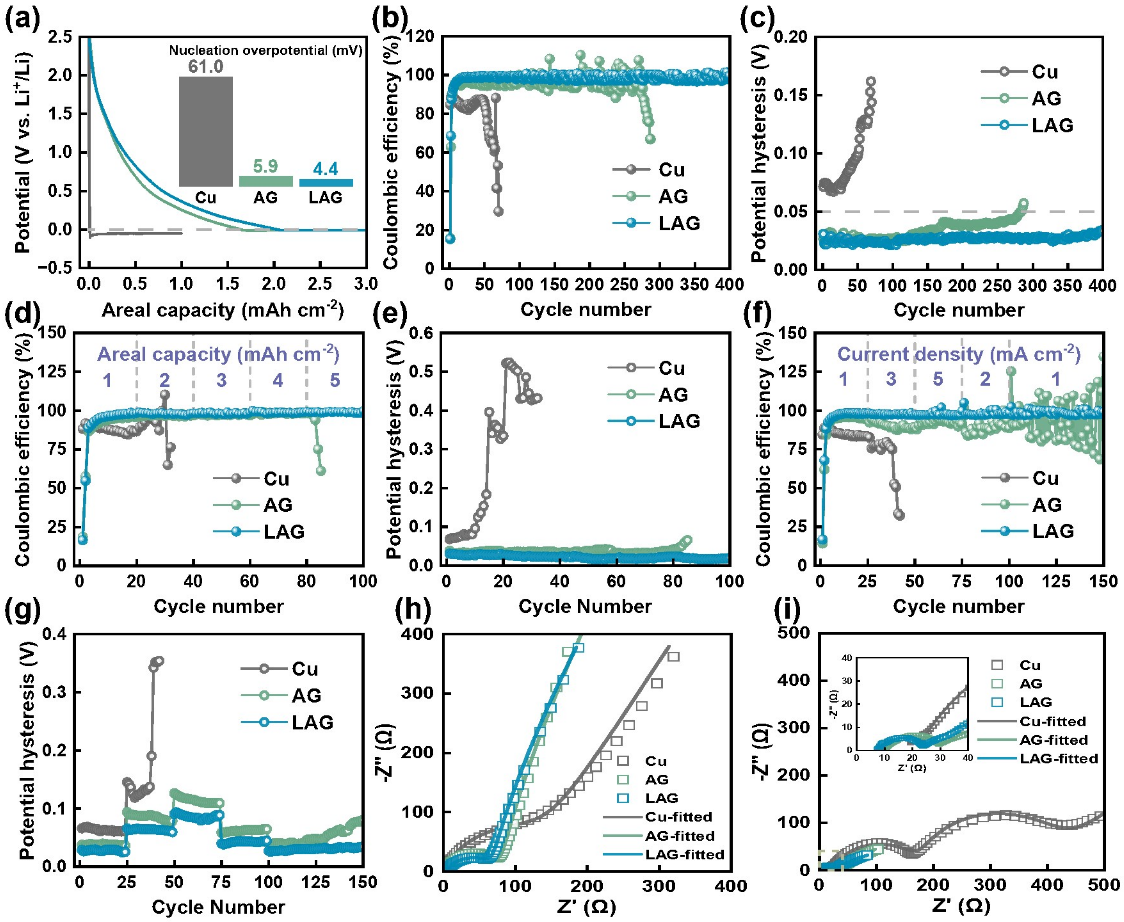

Fig. 3 (a) Lithium plating GCD curves at 0.1 mA cm^{-2} of Cu, AG, and LAG, with the inset image of nucleation overpotentials. Lithium plating/stripping cycling performance of Cu, AG, and LAG at (b, c) 1 mA cm^{-2} and 1 mAh cm^{-2}, (d, e) 1 mA cm^{-2} and 1 to 5 mAh cm^{-2} for each 20 cycles, and (f, g) 1 mAh cm^{-2} and 1 to 5 mA cm^{-2} for each 25 cycles. (h, i) Nyquist plots of before cycling and at SOC = 0 % after 50th cycle (1 mA cm^{-2}, 1 mAh cm^{-2}).

demonstrating the higher reversibility of lithium plating/stripping on LAG.

To further investigate the rate-capacity performance of LAG film during the lithium plating/stripping, the coin half-cells are cycled at various capacities (Fig. 3d and e), and various current densities (Fig. 3f and g). At a moderate current density of 1 mA cm^{-2}, lithium can be plated/stripped reversibly on LAG with capacities from 1 to 5 mAh cm^{-2}. The CE increases and the hysteresis decreases as the capacity increases revealing the good trade-off between the lithium plating/stripping rate and the capacity. As a matter of fact, the CE and hysteresis can reach to ~ 98.9 % and ~ 18.4 mV, respectively, even at a high areal capacity of 5 mA h cm^{-2} (Fig. S15c and d†), which are in fully agreement with the GCD curves showing unique stationary plating/stripping platforms (Fig. S16c and d†). In contrast, the capacity of Cu is below 3 mA h cm^{-2}, and its hysteresis increases quickly over 500 mV. At a capacity of 1 mA h cm^{-2}, LAG shows excellent stability for lithium plating/stripping cycles at varied current densities, the CE remains at ~ 97.6% at a current density of 5 mA cm^{-2} (Fig. S15e and f†). It is known that the electrochemical polarization enlarges as the current density increases, the hysteresis ascends gradually once the current density increasing.[39] However, the hysteresis increasing rate of LAG is much slower than those of AG and Cu. The GCD curves of LAG at different current densities keep consistently, while the AG shows anamorphic GCD curves with highly fluctuating CEs and large ascending hysteresis (Fig. S16e and f†).

The Nyquist plots are acquired and fitted via the equivalent circuit in Fig. S17†. As shown in Fig. 3h and i, the LAG film has also the lowest Li$^+$ transporting resistances across the SEI and charge transfer process resistances before cycling (R_{CT} of 65.9 Ω), and at SOC = 0% after 50th cycle (R_{SEI} of 10.0 Ω and R_{CT} of 5.05 Ω, Table S2†), suggesting the unique interfacial property of the LAG film, due might to the as-decorated with AlN@Li_3N, and MgF_2 particles. The long cycling stability, highly stable CEs, and strong rate-capacity efficiency at large capacity and high current density for lithium plating/stripping, and additionally with the unique porous structure and lithiophilic characteristic make LAG competitive as a host material for lithium plating/stripping.

2.3. Performances of LAG film as host electrode in AL-LMBs.

View Article Online
DOI: 10.1039/D4TA07788A

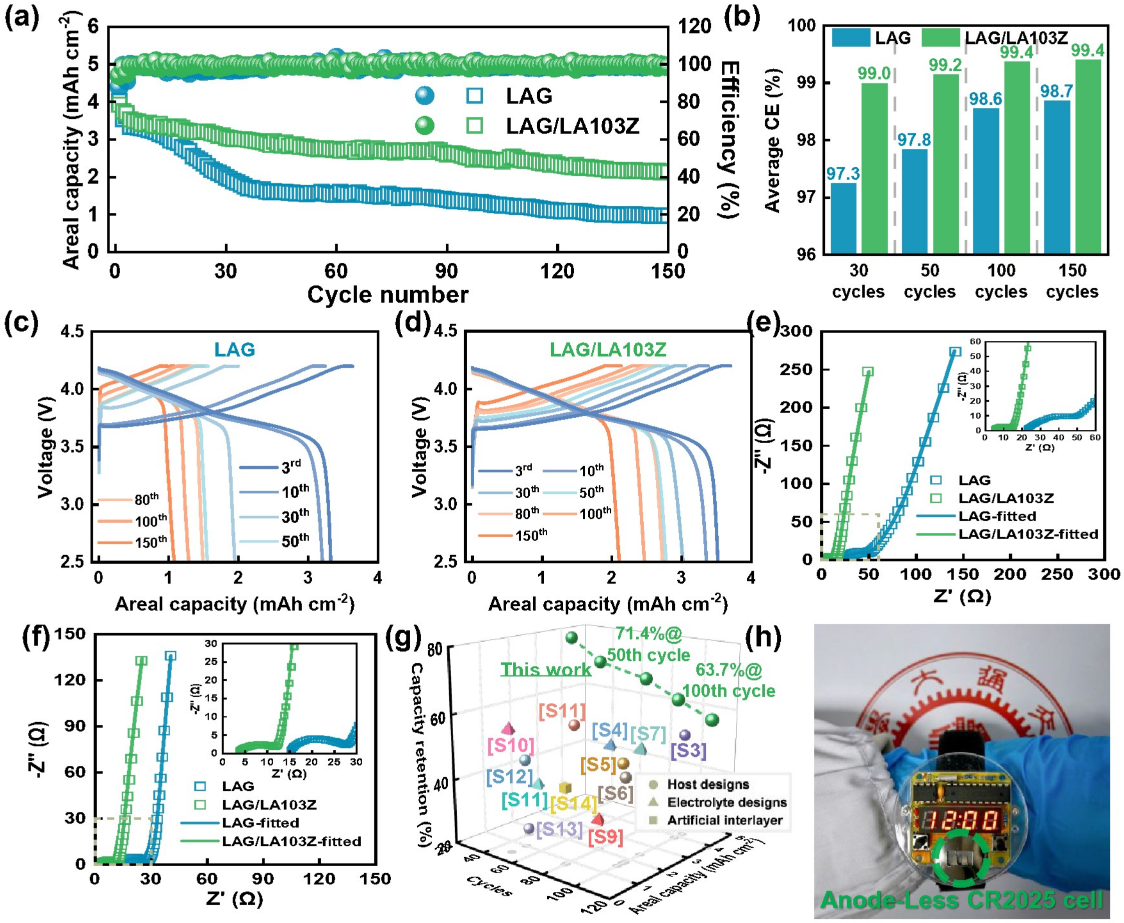

Fig. 4 (a) Charge/discharge cycling performances, (b) average CEs, and (c, d) GCD curves of LAG||NCM811 and LAG/LA103Z||NCM811 cells at 0.5C//0.5C, respectively. (e, f) Nyquist plots of LAG||NCM811 and LAG/LA103Z||NCM811 cells before cycle and at SOC = 0 % after 30th cycle. (g) Comparisons of the electrochemical performance of as-assembled LAG/LA103Z||NCM811 with AL-LMBs reported in literatures. h) Digital photograph of the anode-less CR2025 cell powering an electronic watch (Rated at 0.1 W and 3 V).

Considering the excellent lithium plating/stripping performances demonstrated on coin hall-cells above, a series of full-cells with NCM811 as cathode and LAG as host electrodes for lithium plating/stripping are assembled, and their electrochemical properties are compared. As shown in Fig. 4a, the AL-LMB with LAG as host, LAG||NCM811 cell shows large areal capacity, ~ 3.9 mAh cm^{-2}, using carbonate-based electrolyte containing FEC, but it fades to < 2 mAh cm^{-2} after 30 cycles, indicating the possible lithium loss. To make up for the lithium loss and suppress its effect on the full-cell cycling life, the LAG films are rolled iso-thickly with commercial air-stable Mg-Li alloy foils, LA103Z (consisting of ~ 10 *wt.* % Li, ~ 3 *wt.* % Al, ~ 3 *wt.* % Zn, and ~ 84 *wt.* % Mg, Table S3†) named as LAG/LA103Z film, with the thickness kept at ~ 70 µm. Thus that, as illustrated in Fig. 4b, the LAG/LA103Z||NCM811 cell shows much slower capacity decreasing rate, higher capacity retentions of ~ 60 % after 120 cycles, and the high CE of ~ 99.4 %. These results hint, on the other hand, that the LA103Z foil does make up for the lithium loss, affords the LAG/LA103Z||NCM811 with more stable charge/discharge plateaus over the LAG||NCM811 during continuous cycles (Fig. 4c and d). The Nyquist plots of full-cells are also measured and fitted via the aforementioned equivalent circuit. In Fig. 4e and f, the initial R_{SEI} and R_{CT} of LAG/LA103Z||NCM811 cell are of ~ 10.5 and ~ 13.1 Ω, and lower to ~ 7.8 and ~ 10.9 Ω at SOC = 0 % after 30th cycle (Table S4†), which are much lower than LAG||NCM811 cell as-studied. It exhibits the improved interfacial properties of as-designed integrated bilayer film structure. For comparison, LA103Z||NCM811 cell was also assembles and shows a very continuous rapid capacity descending for <10 cycles, caused by uncontrollable interfacial side-reaction of alloy anodes (Fig. S18†).

Recently, to improve the electrochemical properties of AL-LMBs, the electrolytes with high concentration[40] or high entropy[41] have been utilized. For examples, the AL-LMB using Cu/polymer/Al composite as host electrode, and high concentration electrolyte of 5 M LiFSI and 0.1 M $LiPF_6$ in FEC/DMC/tetrafluoroethyl-tetrafluoropropyl ether (TTE)

View Article Online
DOI: 10.1039/D4TA07788A

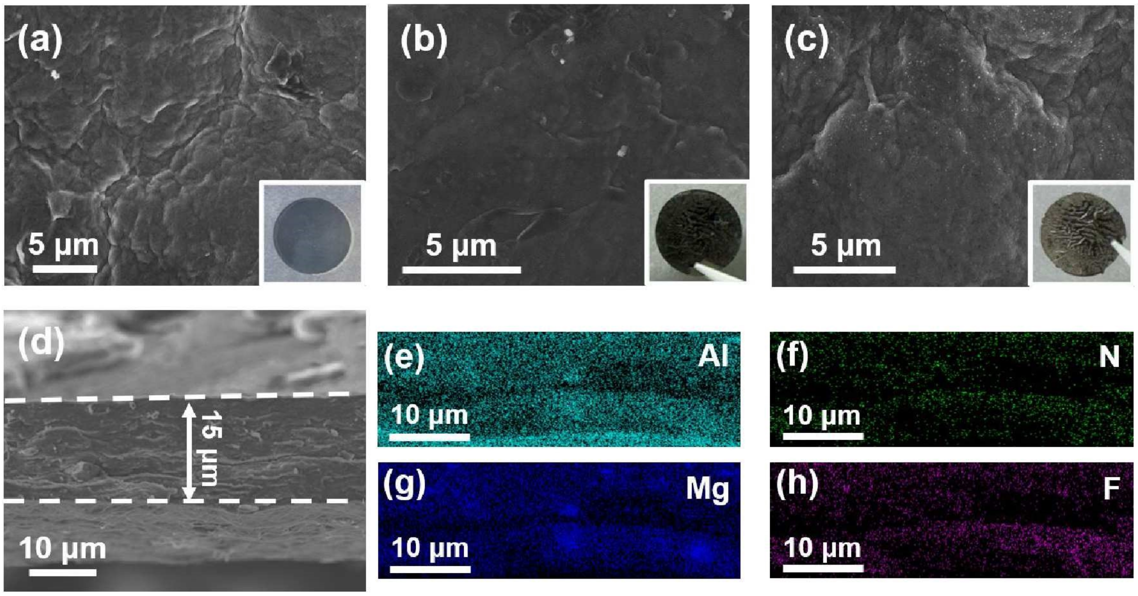

Fig. 5 SEM images of LAG films (a) before cycle, after 30th cycle at (b) SOC = 0 % and (c) SOC = 100 %, with inset optical images of the corresponding electrodes. (d) Cross-sectional SEM image and (e-h) EDS mapping results of LAG film at SOC = 100 % after 30th cycle.

(1/2/2, in volume) delivered a capacity retention of ~50 % after 100 cycles, at the capacity of 1.8 mAh cm^{-2} and current density of 0.9 mA cm^{-2}.[42] In contrast, as aforementioned, the commercial carbonate electrolyte (1 M $LiPF_6$ in EC/DEC/DMC (1/1/1, in volume) with 10 *vol.* % FEC) is used in LAG/LA103Z||NCM811 cell in our work, but the cells still deliver competitive electrochemical performances, including the higher areal capacity, longer cycling stability, and better rate capability. And the comparison details are summarized in Fig. 4g and Table S5†. To look at the effects of the electrolyte on the electrochemical properties of AL-LMB with LAG/LA103Z host electrode, LAG/LA103Z||NCM811 cells are also assembled using the carbonate electrolyte without FEC, and the ether electrolyte (1 M LiTFSI in 1,2-dimethoxyethane (DME) / 1,3-dioxolane (DOL) (1/1, in volume) with 1 wt. % $LiNO_3$), shown in Fig. S19†. The cell using carbonate electrolyte containing no FEC shows lower capacity retentions of ~ 45 % after 100 cycles, due might to the instability of carbonate electrolyte once lack of FEC during lithium plating/stripping cycling.[43, 44] The cell using ether electrolyte has also lower capacity retentions of ~ 50 % after 120 cycles, since the inherent poor electrochemical stability of ether electrolyte under high voltage.[45] In addition, to demonstrate the possible practical application, an electronic watch (rated at 0.1 W and 3 V) is successfully powered with the as-assembled LAG/LA103Z||NCM811cell (Fig. 4h).

2.4. Characterizations on LAG during lithium plating/stripping.

To get insight into the evolutions of as-designed host electrode in AL-LMBs, the morphology variations of LAG films adhered to LA103Z during cycling are characterized using SEM. As depicted in Fig. 5a-c, after 30 cycles of lithium plating/stripping, the surfaces of LAG films are kept well, illustrating the excellent structural stability of LAG against the volumetric fluctuation during lithium plating/stripping. This can explain partially the excellent cycling stability of the AL-LMBs. Further, even at SOC = 100 %, no surficial deposited lithium metal is observed, demonstrating that the lithium plating/stripping should happen within the pores of LAG film. In contrast, during the same lithium plating/stripping, the surface of Cu is destroyed severely, and the irregular lithium dendrites could be detected at SOC = 100 % (Fig. S20†). To localize the exact sites for lithium plating, the cross-sectional SEM images of LAG at SOC = 100 % are acquired. As shown in Fig. 5d, the thickness of LAG film at SOC = 100 % is about 15.1 μm, meaning the compact deposited lithium is homogeneously distributed between graphene sheets. The reason might be from the 3D network motif of LAG which suppresses the large volumetric changes during lithium plating/stripping. The EDS mappings on hetero-elements after lithium plating/stripping are acquired, too. As shown in Fig. 5e-h, the elements including Al, Mg, N, and F are distributed over the LAG, demonstrating that the $AlN@Li_3N$, and MgF_2 particles are loaded tightly onto the graphene sheets during cycling. This is understandable considering that these lithiophilic particles, such as $AlN@Li_3N$ and $MgF_2@LiF$, guide the lithium nucleation and deposition on them. Moreover, ICP-OES results illustrate directly the lithium making up effects of LA103Z foil during cycling, which leads to much enhanced capacity retentions of AL-LMBs (Fig. S21†). In addition, LA103Z foil in LA103Z||NCM811 cell suffers from interfacial side-reactions to a great extent, irreversible lithium plating and stripping with huge and erratic de-alloy reactions, finally leading to uncontrollable structural degeneration (Fig. S22†).

It has been reported that the inorganic SEI components are the key factors affecting the reversible plating/stripping,

View Article Online
DOI: 10.1039/D4TA07788A

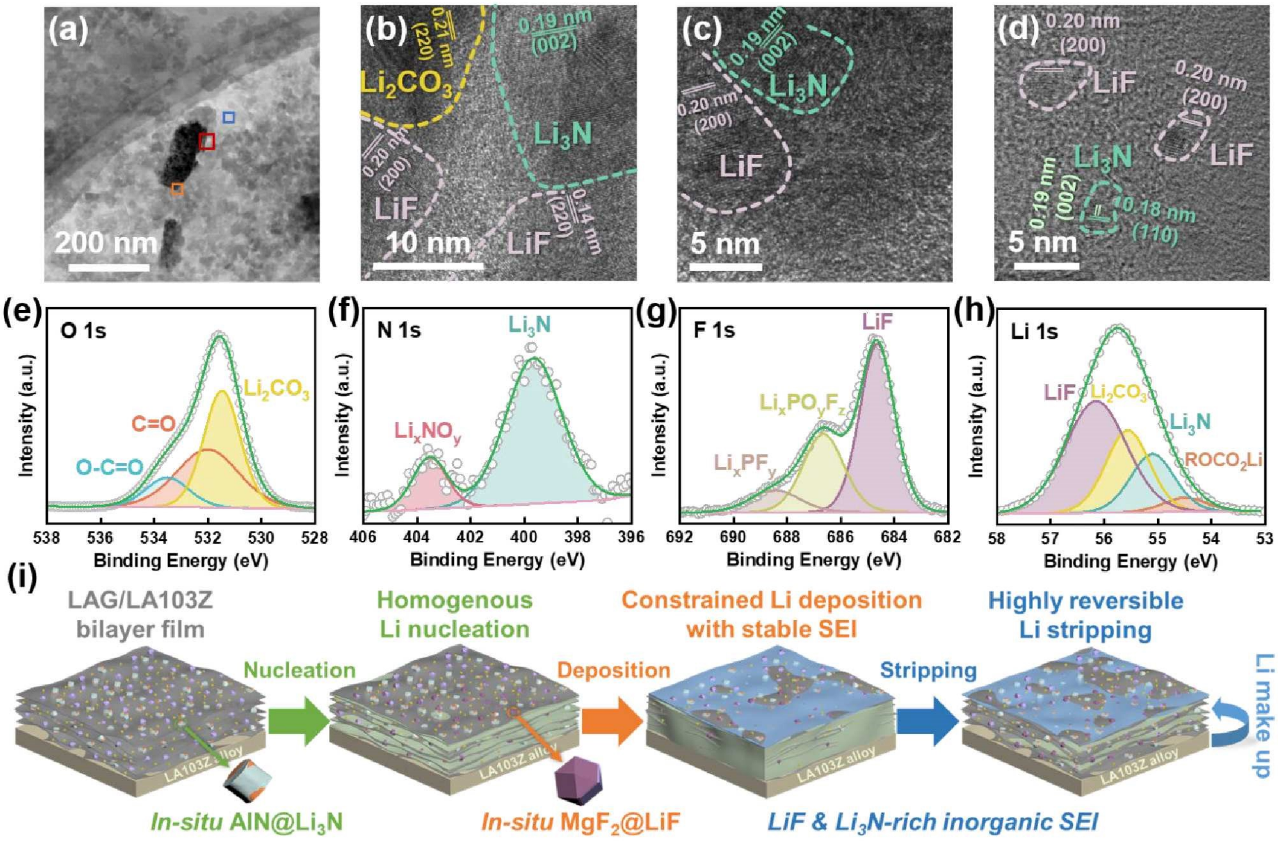

Fig. 6 (a) TEM images of LAG after cycling. (b-d) HRTEM images of the orange, red, and blue sites marked in (a). (e-h) O 1s, N 1s, F 1s, and Li 1s XPS peaks of SEI formed on LAG. (i) Schematic illustrations of the morphological and interfacial evolutions of LAG film.

among which the LiF and Li_3N have been recognized as favorable inorganic components in SEI.[46, 47] To elucidate the composition of the SEI formed on LAG, TEM and XPS data are collected after lithium plating/stripping. As illustrated in Fig. 6a, TEM images show that there are nanoparticles distributed uniformly on graphene sheets. The HRTEM images of those nanoparticles, Fig. 6b-d, demonstrate that the lattices parameters of the nanoparticles are of 0.20 and 0.14 nm corresponding to the $d_{(200)}$ and $d_{(220)}$ of LiF, 0.19 and 0.25 nm matching to the $d_{(002)}$ and $d_{(110)}$ of Li_3N, and 0.21 nm consisting with $d_{(220)}$ of Li_2CO_3.[48, 49] The loaded AlN particles are still observed on graphene sheets (Fig. S23†). However, no lattice d-spaces of MgF_2 particles are detected, the reason might be that the as-decorated MgF_2 particles have been converted to LiF during the lithium plating/stripping.

To quantitatively analyse the chemical compositions of the SEI formed on LAG, XPS measurements are conducted. The O 1s spectrum is deconvoluted, the hyperfine peaks at 532 and 533.5 eV are corresponded with C=O and O-C=O, separately (Fig. 6e). Those species are mainly attributed to decomposition of carbonate electrolyte to $ROCO_2$-Li species as dominant organic SEI components. And Li_2CO_3 (531.5 eV) is an essential inorganic SEI component. Thus, the SEI represents more inorganic but less organic species, which the C 1s spectrum also proves (Fig. S24†). Fig. 6f shows the N 1s spectrum of the SEI. Clearly, a peak at 399.8 eV is detected due might to the *in-situ* formation of Li_3N from the loaded AlN during lithium plating/stripping. Fig. 6g depicts the F 1s spectrum, the peaks at 688.5 and 686.8 eV are contributed to Li_xPF_y and $Li_xPO_yF_z$ originated from the decomposition of $LiPF_6$. The less contents of them account for the SEI might protect $LiPF_6$ from the further side-reactions. [50, 51] The peak at 684.7 eV is from LiF, suggesting the formation of a LiF-rich SEI on LAG. From Li 1s peaks shown in Fig. 6h, it can be deduced that considerable contents of LiF (56.2 eV) and Li_3N (55.1 eV) are obtained. The calculated atomic proportions of XPS spectra of the SEI are summarized in Table S6†. Specifically, the results show that the pre-loaded AlN and MgF_2 particles can enhance the formation of LiF and Li_3N enriched SEI on LAG host electrode surface. Additionally, the as-formed LiF and Li_3N-rich inorganic SEI should facilitate the Li^+ transportation, weaken the solvation coordination of solvated Li^+, and reduce the interfacial resistance.[33, 34, 47]

Based on the aforementioned analysis, the morphological and interfacial evolutions of LAG film facing the electrolyte during lithium plating/stripping cycling are proposed schematically in Fig. 6i. The homogenous nucleation occurs on the LAG film, induced by lithiophilic *in-situ* AlN@Li_3N and MgF_2@LiF, which guides the lithium deposition among graphene sheets, and highly reversible lithium stripping almost

View Article Online
DOI: 10.1039/D4TA07788A

without residue caused by benign structure of deposited lithium. Meanwhile, LiF and Li_3N-rich inorganic SEI formed *in-situ* on LAG can protect the as-deposited lithium, and even facilitates lithium plating/stripping cycling, while the LA103Z can continuously make up for the lithium loss.

3. Conclusions

The free-standing porous graphene films decorated with the lithiophilic particles of AlN@Li_3N, MgF_2, and Li_2CO_3, and the LA103Z foil are designed and fabricated as the host electrodes for AL-LMBs. The alkalization, AlN and MgF_2 loading, and fast thermal reduction afford the as-prepared films with highly reversible and stable lithium plating/stripping performance at a current density of 5 mA cm^{-2} and a capacity of 5 mAh cm^{-2}. Specifically, the thin LA103Z foil can make up for the lithium loss during long-term lithium plating/stripping. The pre-loaded AlN@Li_3N and MgF_2 can enhance the formation of LiF and Li_3N-rich inorganic SEI which suppresses the side-reactions involved the electrolyte, facilitates the Li^+ transport, promotes the Li^+ desolvation, reduces the interfacial resistance, and stabilizes the lithium plating/stripping. Having the unique composition and morphology, the AL-LMB assembled with LAG film adhered with LA103Z foil as host electrode and NCM811 as cathode, LAG/LA103Z||NCM811, can deliver the capacity retentions of ~ 60 % after 120 cycles at 3.86 mAh cm^{-2} and 1.93 mA cm^{-2} in carbonate-based electrolyte. This work hopefully puts forward the practical application of free-standing graphene films as host electrodes in high-performance AL-LMBs.

4. Experimental Section

4.1 Material preparation.

GO powders were purchased from Xi'an Times Graphene New Energy Technology Co., Ltd. (Shaanxi, China). The GO was suspended in deionized water under ultrasonication for 30 min and then stirring for 24 h to get the GO precursor solution of 3 mg mL^{-1}. Prior to decoration with inorganic particles, the GO was alkalized by adding LiOH in GO solution until the LiOH concentration reaching to 0.1 M (pH = 13). The AlN and MgF_2 particles were decorated on the GO sheets by mixing the corresponding particles with the alkalized GO solution, then vacuum filtered using cellulose membranes with diameter and aperture of 50 and 0.22 μm. The mass ratios of AlN and MgF_2 to GO are kept less than 1:10 to reduce their effects on the thin film formation. The as-obtained films were washed fully with ethyl alcohol (95 %), dried at 50°C for 20 min, and then further annealed at 500 °C for 30 min with the heating rates of ~ 50 °C s^{-1}. During the procedure, the GO was reduced, and the thin films were named as AG and LAG, with and without inorganic particles, respectively. All thermal reduction processes were conducted in air atmosphere, using a tube furnace (Hefei Kejing Materials Technology Co., Ltd., Anhui, China).

Mg-Li alloy foil with thickness of 50 μm, known as LA103Z, was purchased from Suzhou Xinghai Electronic Business Co., Ltd (Jiangsu, China). The LA103Z foil was first pickled in chromic acid solution (90 g L^{-1} of CrO_3, and 25 g L^{-1} of $LiNO_3$ aqueous solution) for ~ 3 min, and then was fully cleaned under ultrasonication in ultrapure water and ethyl alcohol (95 %), until white metallic surface was observed. The LAG film and pickled LA103Z foil was rolled together at 50 °C on an electric roller (Hefei Kejing Materials Technology Co., Ltd., Anhui, China) to get the LAG/LA103Z bilayer film.

4.2 Characterizations.

X-ray microscopy (XRM) images were obtained on an Xradia 520 Versa X-ray microscope (Carl Zeiss, Germany), operated at an accelerating voltage of 80 kV, and a voxel resolution of 0.5052 μm. The 3D-reconstruction of the XRM images were processed using Dragonfly Pro software (Comet Technologies Canada Inc.) based on density. Scanning electron microscopy (SEM) images and energy-dispersive X-ray spectroscopy (EDS) data were acquired using a NOVA NanoSEM 230 field emission scanning electron microscope (Thermo Fisher Scientific, U. S. A). The top-view SEM images were recorded on back scattered electrons mode, while the secondary electrons were used for the cross-sectional (side-view) imaging.

Transmission electron microscopy (TEM) and high-resolution TEM (HRTEM) images were obtained on a Talos F200X field emission transmission electron microscope (Thermo Fisher Scientific, U. S. A). For TEM imaging, the film was grounded and dispersed into dimethyl carbonate (DMC), then loaded onto the TEM grid. HRTEM were operated at an accelerating voltage of 200 kV. X-ray diffraction (XRD) patterns were obtained on an Aeris metals edition X-ray diffractometer (Malvern Panalytical, China) with Cu K_α irradiation (λ = 0.154 nm), at a scanning rate of 2 ° min^{-1}. X-ray photoelectron spectroscopy (XPS) measurements were conducted on an EscaLab Xi+ X-ray photoelectron spectrometer (Thermo Fisher Scientific, U. S. A). All XPS spectra were calibrated using the 284.8 eV of C 1s of C–C/C-H peak as reference. Thermogravimetric analysis (TGA) was performed from room temperature to 700 °C at a heating rated of 10 °C min^{-1} in air atmosphere on a TGA8000 instrument (PerkinElmer, U. S. A). Since Li_2CO_3 is introduced through the alkalization process and the component differences between the AG and LAG films are AlN@Li_3N and MgF_2, the mass ratio of Li_2CO_3 is calculated by the difference between AG and GO ash remnants, while the mass ratios of AlN@Li_3N and MgF_2 by the difference between LAG and AG ash remnants. Raman spectra were obtained using an inVia Qontor (Renishaw, U. K.) at an excitation laser wavelength of 532 nm. The Attenuated Total Reflection Infrared (ATR-IR) spectra were acquired on an EQUINOX 55 FTIR spectrometer (Bruker, Germany).

Zeta potentials were measured in water, 0.1 M LiOH aqueous solution, and DMC, using a Zetasizer Nano ZSE instrument (Malvern Panalytical, China). The samples for zeta-potential measurements were prepared by suspending the solid particles into liquid phase at a concentration 0.5 mg mL^{-1}. The particle size distributions of AlN and MgF_2 were evaluated on a Mastersizer 3000 instrument (Malvern Panalytical, China). Nitrogen adsorption analysis was

View Article Online
DOI: 10.1039/D4TA07788A

conducted at 77.35 K using an ASAP2460 aperture analyzer (Micromeritics, U. S. A). To avoid false peaks at ~ 3.8 nm in desorption curves, BJH analyses were all based on adsorption curves. Tensile stress-strain tests were operated on a Discovery DMA800 instrument (TA Instruments-Waters LLC, U. S. A). Contact-angle were measured with water and DMC (5 μL) on a DSA100 instrument (Kruss, Germany). Inductively coupled plasma optical emission spectroscopy (ICP-OES) measurements were conducted on an Avio 500 spectrometer (PerkinElmer, Singapore). For the XPS, SEM, TEM, and ICP-OES measurements on the electrodes after lithium plating and stripping cycle, the bilayer thin films were fully rinsed with DMC to remove the residual electrolyte. The preparation and transference of the cycled electrodes were conducted in an argon-filled glovebox to avoid effects of oxygen and water vapor in air.

4.3 Electrochemical measurements.

All electrochemical measurements were carried out on CR2025 coin cells assembled in a glove box filled with argon. For half-cell cycle assemble, the as-prepared thin bilayer films were cut into disks of 12 mm in diameter as working electrodes, the commercial Li foil (16 mm in diameter, and ~ 100 μm in thickness) was used as countered electrodes, 1 M $LiPF_6$ in ethylene carbonate (EC) /diethyl carbonate (DEC) /dimethyl carbonate (DMC) (1/1/1, in *vol.*) with 10 *vol.* % fluoroethylene carbonate (FEC) as the electrolyte. To get a proper average CE, the initial 5 cycles were excluded to better judge lithium plating and stripping reversibility.[39, 52] The constant current lithium plating (discharging) and stripping (charging) mode was chosen for coin half-cell cycling.

The full cells were constructed with Cu, LAG, and LAG/LA103Z as host electrodes, and NCM811 as cathode. Before full-cell assembly, LAG, and LAG/LA103Z were pre-cycled in half-cells between 0.01 and 1 V, to eliminating initial irreversible lithium consumption, but maintained at delithiation state without excess lithium.[52, 53] The loading mass of NCM811 on cathode was 20 mg cm^{-2}, with the areal capacity of 3.86 mAh cm^{-2}. The electrolyte used in the full-cell is the same as that used in the half-cell. Celegard 2400 film was used as the separator. All full-cells were charged and discharged at 0.05C (0.193 mA cm^{-2}) for initial 2 cycles, then charged at 0.5C (1.93 mA cm^{-2}) to 4.2 V, with constant-voltage charging at 4.2 V until current decreasing to 0.05C, then discharged at 0.5C to 2.5 V. The electrochemical impedance spectroscopy (EIS) data were collected by applying a perturbation voltage of 5 mV versus the open-circuit potential in a frequency range from 10^6 to 0.01 Hz. All galvanostatic charge-discharge (GCD) curves were measured on a LAND-CT2001A electrochemical workstation (Wuhan LAND, China), while CV and EIS datas were acquired on an AUTOLAB electrochemical workstation (Metrohm, Switzerland)

Author contributions

Mingliang Bai: conceptualization, data curation, formal analysis, investigation, methodology, writing – original draft. Min Zhong: funding acquisition, methodology, resources, supervision, writing – review & editing. Wenzhuo Shen: funding acquisition, resources. Jiali Zhang: funding acquisition, resources. Shouwu Guo: funding acquisition, methodology, resources, supervision, writing – review & editing.

Conflicts of interest

There are no conflicts to declare.

Data availability

The data supporting this article have been included as part of the Supplementary Information.

Acknowledgements

The authors also wish to express their appreciation to the Instrument Analysis Centre of SJTU. We are grateful for the discussion about the XPS data with Ms. Xue Ding and XRM data with Ms. Yanhua Zhu in the Instrumental Analysis Centre of Shanghai Jiao Tong University.

References

1. A. Masias, J. Marcicki and W. A. Paxton, *ACS Energy Lett.*, 2021, **6**, 621-630.
2. H. Li, *Joule*, 2019, **3**, 911-914.
3. P. Albertus, V. Anandan, C. Ban, N. Balsara, I. Belharouak, J. Buettner-Garrett, Z. Chen, C. Daniel, M. Doeff, N. J. Dudney, B. Dunn, S. J. Harris, S. Herle, E. Herbert, S. Kalnaus, J. A. Libera, D. Lu, S. Martin, B. D. McCloskey, M. T. McDowell, Y. S. Meng, J. Nanda, J. Sakamoto, E. C. Self, S. Tepavcevic, E. Wachsman, C. Wang, A. S. Westover, J. Xiao and T. Yersak, *ACS Energy Lett.*, 2021, **6**, 1399-1404.
4. W. Xu, J. Wang, F. Ding, X. Chen, E. Nasybulin, Y. Zhang and J.-G. Zhang, *Energy Environ. Sci.*, 2014, **7**, 513-537.
5. M. Yeddala, L. Rynearson and B. L. Lucht, *ACS Energy Lett.*, 2023, **8**, 4782-4793.
6. C.-J. Huang, H.-C. Tao, P.-J. Chao, C.-Y. Li, B. T. Hotasi, H.-Y. Liu, M.-H. Lin, S.-H. Wu, W.-N. Su and B. J. Hwang, *ACS Nano*, 2023, **17**, 13241-13255.
7. A. J. Sanchez and N. P. Dasgupta, *J. Am. Chem. Soc.*, 2024, **146**, 4282-4300.
8. T. T. K. Ingber, M. M. Bela, F. Püttmann, J. F. Dohmann, P. Bieker, M. Börner, M. Winter and M. C. Stan, *J. Mater. Chem. A*, 2023, **11**, 17828-17840.
9. C. Liu, B. Wu, Y. Zhang, T. Liu, J. Cui, L. Huang, G. Tan, L. Zhang, Y. Su and F. Wu, *J. Mater. Chem. A*, 2023, **11**, 25455-25464.
10. Z. Tong, B. Bazri, S.-F. Hu and R.-S. Liu, *J. Mater. Chem. A*, 2021, **9**, 7396-7406.
11. P. Liu, S. Shen, Z. Qiu, T. Yang, Y. Liu, H. Su, Y. Zhang, J. Li, F. Cao, Y. Zhong, X. Liang, M. Chen, X. He, Y. Xia, C. Wang, W. Wan, J. Tu, W. Zhang and X. Xia, *Adv. Mater.*, 2024, **36**, 2312812.
12. R. M. Kasse, N. R. Geise, J. S. Ko, J. Nelson Weker, H.-G. Steinrück and M. F. Toney, *J. Mater. Chem. A*, 2020, **8**, 16960-16972.
13. P. Ma, R. Kumar, M. C. Vu, K.-H. Wang, P. Mirmira and C. V. Amanchukwu, *J. Mater. Chem. A*, 2024, **12**, 2479-2490.

View Article Online
DOI: 10.1039/D4TA07788A

14. A. J. Louli, A. Eldesoky, R. Weber, M. Genovese, M. Coon, J. deGooyer, Z. Deng, R. T. White, J. Lee, T. Rodgers, R. Petibon, S. Hy, S. J. H. Cheng and J. R. Dahn, *Nat. Energy*, 2020, **5**, 693-702.
15. D. Wang, J. Qiu, N. Inui, R. Hagiwara, J. Hwang and K. Matsumoto, *ACS Energy Lett.*, 2023, **8**, 5248-5252.
16. K. B. Hatzell, *ACS Energy Lett.*, 2023, **8**, 4775-4776.
17. J.-J. Woo, V. A. Maroni, G. Liu, J. T. Vaughey, D. J. Gosztola, K. Amine and Z. Zhang, *J. Electrochem. Soc.*, 2014, **161**, A827.
18. T. Lyu, F. Luo, D. Wang, L. Bu, L. Tao and Z. Zheng, *Adv. Energy Mater.*, 2022, **12**, 2201493.
19. Q. Zhang, L. Xu, X. Yue, J. Liu, X. Wang, X. He, Z. Shi, S. Niu, W. Gao, C. Cheng and Z. Liang, *Adv. Energy Mater.*, 2023, **13**, 2302620.
20. D. W. Kang, S. S. Park, H. J. Choi, J.-H. Park, J. H. Lee, S.-M. Lee, J.-H. Choi, J. Moon and B. G. Kim, *ACS Nano*, 2022, **16**, 11892-11901.
21. S. Zhang, S. Xiao, D. Li, J. Liao, F. Ji, H. Liu and L. Ci, *Energy Storage Mater.*, 2022, **48**, 172-190.
22. T. Yang, L. Li, F. Wu and R. Chen, *Adv. Funct. Mater.*, 2020, **30**, 2002013.
23. C. Gao, J. Kang, Y. Zhang, C. He, C. Shi, B. Chen, L. Ma, E. Liu, J. Sha, F. Zhou and N. Zhao, *Chem. Commun.*, 2024, **60**, 9130-9148.
24. T. Li, Z. Qiu, T. Zhang, H. Liao, C. Li, B. Ye, Q. Xiong, Y. Zhang and X. Xia, *Electrochim. Acta*, 2024, **494**, 144427.
25. K. Lin, X. Qin, M. Liu, X. Xu, G. Liang, J. Wu, F. Kang, G. Chen and B. Li, *Adv. Funct. Mater.*, 2019, **29**, 1903229.
26. H. Chen, Y. Yang, D. T. Boyle, Y. K. Jeong, R. Xu, L. S. de Vasconcelos, Z. Huang, H. Wang, H. Wang, W. Huang, H. Li, J. Wang, H. Gu, R. Matsumoto, K. Motohashi, Y. Nakayama, K. Zhao and Y. Cui, *Nat. Energy*, 2021, **6**, 790-798.
27. H. Yao, F. Niu, C. Ma, X. You, D. Ning, J. Qian, M. Wang, Q. Duan, C. Yang, Q. Wu, J. Wang, J. Zhang, Z. Lu, C. Yang and W. Wu, *Adv. Funct. Mater.*, 2024, **34**, 2310711.
28. K. Kim and Y. Lee, *Nuclear Engineering and Technology*, 2021, **53**, 2341-2347.
29. D. X. Wu, J. He, J. D. Liu, M. G. Wu, S. A. Qi, H. P. Wang, J. D. Huang, F. Li, D. L. Tang and J. M. Ma, *Advanced Energy Materials*, 2022, **12**.
30. X. Chen, W. Li, D. Luo, M. Huang, X. Wu, Y. Huang, S. H. Lee, X. Chen and R. S. Ruoff, *ACS Nano*, 2017, **11**, 665-674.
31. X. Chen, D. Meng, B. Wang, B.-W. Li, W. Li, C. W. Bielawski and R. S. Ruoff, *Carbon*, 2016, **101**, 71-76.
32. M. H. Brooker and J. Wang, *Spectrochimica Acta Part A: Molecular Spectroscopy*, 1992, **48**, 999-1008.
33. H. Wan, J. Xu and C. Wang, *Nat. Rev. Chem.*, 2024, **8**, 30-44.
34. M. S. Kim, Z. Zhang, J. Wang, S. T. Oyakhire, S. C. Kim, Z. Yu, Y. Chen, D. T. Boyle, Y. Ye, Z. Huang, W. Zhang, R. Xu, P. Sayavong, S. F. Bent, J. Qin, Z. Bao and Y. Cui, *ACS Nano*, 2023, **17**, 3168-3180.
35. K. Yan, Z. Lu, H.-W. Lee, F. Xiong, P.-C. Hsu, Y. Li, J. Zhao, S. Chu and Y. Cui, *Nat. Energy*, 2016, **1**, 16010.
36. X.-R. Chen, B.-C. Zhao, C. Yan and Q. Zhang, *Adv. Mater.*, 2021, **33**, 2004128.
37. H.-S. Lim, D. T. Nguyen, J. A. Lochala, X. Cao and J.-G. Zhang, *ACS Energy Lett.*, 2024, **9**, 126-135.
38. P. Peljo and H. H. Girault, *Energy Environ. Sci.*, 2018, **11**, 2306-2309.
39. S. Cho, D. Y. Kim, J.-I. Lee, J. Kang, H. Lee, G. Kim, D.-H. Seo and S. Park, *Adv. Funct. Mater.*, 2022, **32**, 2208629.
40. W. Chen, R. V. Salvatierra, M. Ren, J. Chen, M. G. Stanford and J. M. Tour, *Adv. Mater.*, 2020, **32**, 2002850.
41. S. C. Kim, J. Wang, R. Xu, P. Zhang, Y. Chen, Z. Huang, Y. Yang, Z. Yu, S. T. Oyakhire, W. Zhang, L. C. Greenburg, M. S. Kim, D. T. Boyle, P. Sayavong, Y. Ye, J. Qin, Z. Bao and Y. Cui, *Nat. Energy*, 2023, **8**, 814-826.
42. X. Liao, X. Wang, C. Yan, B. Zhang, Y. Ni, H. Yuan, Y. Pan, J. a. Pan and J. Huang, *Adv. Funct. Mater.*, 2024, DOI: 10.1002/adfm.202310925, 2310925.
43. X.-Q. Zhang, X.-B. Cheng, X. Chen, C. Yan and Q. Zhang, *Adv. Funct. Mater.*, 2017, **27**, 1605989.
44. Y. Zhang, F. Li, Y. Cao, M. Yang, X. Han, Y. Ji, K. Chen, L. Liang, J. Sun and G. Hou, *Adv. Funct. Mater.*, 2024, **34**, 2315527.
45. Z. Jiang, T. Yang, C. Li, J. Zou, H. Yang, Q. Zhang and Y. Li, *Adv. Funct. Mater.*, 2023, **33**, 2306868.
46. S. Zhang, R. Li, N. Hu, T. Deng, S. Weng, Z. Wu, D. Lu, H. Zhang, J. Zhang, X. Wang, L. Chen, L. Fan and X. Fan, *Nat. Commun.*, 2022, **13**, 5431.
47. J. Tan, J. Matz, P. Dong, J. Shen and M. Ye, *Adv. Energy Mater.*, 2021, **11**, 2100046.
48. Y.-H. Tan, Z. Liu, J.-H. Zheng, Z.-J. Ju, X.-Y. He, W. Hao, Y.-C. Wu, W.-S. Xu, H.-J. Zhang, G.-Q. Li, L.-S. Zhou, F. Zhou, X. Tao, H.-B. Yao and Z. Liang, *Adv. Mater.*, 2024, **36**, 2404815.
49. C. Ma, Q. Qiao, K. Yue, J. Yue, X. Cai, J. Zheng, L. Kang, Y. Wang, J. Nai, J. Luo, H. Yuan, S. Zou, X. Tao and Y. Liu, *Adv. Funct. Mater.*, 2024, DOI: 10.1002/adfm.202406479, 2406479.
50. E. W. C. Spotte-Smith, T. B. Petrocelli, H. D. Patel, S. M. Blau and K. A. Persson, *ACS Energy Lett.*, 2023, **8**, 347-355.
51. G.-X. Li, H. Jiang, R. Kou, D. Wang, A. Nguyen, M. Liao, P. Shi, A. Silver and D. Wang, *ACS Energy Lett.*, 2022, **7**, 2282-2288.
52. C. Cui, C. Yang, N. Eidson, J. Chen, F. Han, L. Chen, C. Luo, P.-F. Wang, X. Fan and C. Wang, *Adv. Mater.*, 2020, **32**, 1906427.
53. C. Wang, M. Liu, M. Thijs, F. G. B. Ooms, S. Ganapathy and M. Wagemaker, *Nat. Commun.*, 2021, **12**, 6536.

View Article Online
DOI: 10.1039/D4TA07788A

Data Availability Statement

The data supporting this article have been included as part of the Supplementary Information.